INTERNATIONAL JOURNAL FOR NUMERICAL METHODS IN FLUIDS, VOL. 21, 667–681 (1995)

INTRODUCTION OF TURBULENT MODEL IN A MIXED FINITE VOLUME/FINITE ELEMENT METHOD

C. LE RIBAULT, M. BUFFAT AND D. JEANDEL

Laboratoire de Mécanique des Fluides et d'Acoustique ECL, UCB, CNRS URA 263, 36, avenue Guy de Collongue BP 163 69131 Ecully Cedex, France

SUMMARY

The aim of this work is to present a new numerical method to compute turbulent flows in complex configurations. With this in view, a k-ε model with wall functions has been introduced in a mixed finite volume/finite element method. The numerical method has been developed to deal with compressible flows but is also able to compute nearly incompressible flows. The physical model and the numerical method are first described, then validation results for an incompressible flow over a backward-facing step and for a supersonic flow over a compression ramp are presented. Comparisons are performed with experimental data and with other numerical results. These simulations show the ability of the present method to predict turbulent flows, and this method will be applied to simulate complex industrial flows (flow inside the combustion chamber of gas turbine engines). The main goal of this paper is not to test turbulence models, but to show that this numerical method is a solid base to introduce more sophisticated turbulence model.

KEY WORDS: mixed finite element/finite volume method; flux splitting techniques; compressible turbulent flows; k-ε model; wall functions.

1. INTRODUCTION

With the advent of high speed computers, numerical simulations of compressible flows in complex geometries are becoming of interest for various engineering applications.[1] Practical high speed flows, however, are usually turbulent and thus efficient numerical methods with suitable turbulence models must be selected to simulate these flows accurately. The algebraic eddy viscosity models still represent a common choice[1–3] for compressible simulations since their implementation results generally in the minimum requirement of computer time and storage, but they lack generality especially for the prediction of internal flows in presence of more than one wall. Evaluations of different one point closure turbulent models[4] (zero, one and two equations models) have shown that there was no apparent superiority of one of those models over the others. Some models seemed superior for specific experimental test cases and inferior for others. The main advantage of the two equations model is that, for the general case when the length scale is not known, the k-ε type models provide a more general formulation and now are engineering standard. Then, to describe turbulent flows, a k-ε model initially developed by Launder and Spalding[5] for incompressible flows has been chosen. The model is only valid for large Reynolds number flows and thus must be modified in the vinicity of solid boundaries. To avoid the use of a low Reynolds number model, which requires a considerable number of mesh nodes in the vicinity of the wall, wall functions[6] are introduced as boundary conditions at a small distance from the wall.

To compute supersonic flows with shocks, the numerical scheme should achieve a precise balance of a typically very small physical diffusion and of a numerical diffusion required for stability. Many

CCC 0271–2091/95/080667–15

Received April 1992
Revised March 1995

studies have been done for the solution of the Euler and Navier–Stokes equations[7–9] and have led to the development of efficient solvers. Furthermore, due to the ease with which complex geometries can be handled and due to the possibility of enhancing the solution accuracy through local mesh refinements,[10,11] we have chosen to use unstructured meshes. Thus, a mixed finite volume/finite element method, developed by Dervieux[12,13] to solve the Euler and Navier–Stokes equations on unstructured meshes, is used. The stabilization of both acoustic and convective waves is realised by applying a flux splitting technique introduced by Roe.[9,14] The success of this method to solve compressible Euler flows stimulates us to extend it to turbulent flows using a k-ε model with wall functions.

In the first part, the physical model and the governing equations are detailed. In the second part, the numerical method and the introduction of the k-ε model and boundary treatment are presented. Finally, two classical validations cases are presented: an incompressible flow over a backward-facing step and an interaction of an oblique shock wave, produced by a ramp, and a turbulent boundary layer. In the two cases, the numerical results are compared with experimental and numerical data.

2. GOVERNING EQUATIONS AND BOUNDARY CONDITIONS

2.1. *Mean Navier–Stokes equations*

The governing equations of the mean flow are obtained by Reynolds averaging the Navier–Stokes equations using a Reynolds average (denoted by an overbar) for the density ρ and the total energy E and a Favre average (denoted by a tilde) for the velocity. To solve the closure problem introduced by this averaging, the Reynolds stress and the turbulent heat flux are modelled using a Boussinesq hypothesis:

$$-\bar{\rho}\widetilde{u_i''u_j''} = \mu_t\left(\frac{\partial \tilde{u}_i}{\partial x_j} + \frac{\partial \tilde{u}_j}{\partial x_i} - \frac{2}{3}\frac{\partial \tilde{u}_k}{\partial x_k}\delta_{ij}\right) - \frac{2}{3}\bar{\rho}\tilde{k}\delta_{ij}. \tag{1}$$

The turbulent viscosity μ_t is defined as a function of two local turbulent scales: for the k-ε model, the turbulent kinetic energy $\tilde{k}$ and its dissipation rate $\tilde{\varepsilon}$. In two dimensions, the non-dimensional Navier–Stokes equations for the mean quantities are written in conservative form:

$$\frac{\partial W}{\partial t} + \operatorname{div}(F) = \operatorname{div}(R), \tag{2}$$

where W represents the mean quantities, $F = [F_1, F_2]$ the convective fluxes and $R = [R_1, R_2]$ the diffusive and turbulent fluxes vector

$$W = \begin{pmatrix} \bar{\rho} \\ \bar{\rho}\tilde{u}_1 \\ \bar{\rho}\tilde{u}_2 \\ \bar{E} \end{pmatrix}, \quad F_1 = \begin{pmatrix} \bar{\rho}\tilde{u}_1 \\ \bar{\rho}\tilde{u}_1^2 + \bar{p} + \frac{2}{3}\bar{\rho}\tilde{k} \\ \bar{\rho}\tilde{u}_1\tilde{u}_2 \\ (\bar{E} + \bar{p} + \frac{2}{3}\bar{\rho}\tilde{k})\tilde{u}_1 \end{pmatrix}, \quad F_2 = \begin{pmatrix} \bar{\rho}\tilde{u}_2 \\ \bar{\rho}\tilde{u}_1\tilde{u}_2 \\ \bar{\rho}\tilde{u}_2^2 + \bar{p} + \frac{2}{3}\bar{\rho}\tilde{k} \\ (\bar{E} + \bar{p} + \frac{2}{3}\bar{\rho}\tilde{k})\tilde{u}_2 \end{pmatrix}, \tag{3}$$

where $\bar{\rho}$ denotes the fluid mean density, $\tilde{u}_1$ and $\tilde{u}_2$ the x and y components of the Favre averaged velocity and $\bar{E}$ the mean total energy. The mean pressure $\bar{p}$ is calculated from the state equation of a perfect gas:

$$\bar{p} = (\gamma - 1)\left(\bar{E} - \bar{\rho}\frac{\tilde{u}_1^2 + \tilde{u}_2^2}{2} - \bar{\rho}\tilde{k}\right) \tag{4}$$

The diffusive and turbulent fluxes R are given by:

$$R_1 = \begin{pmatrix} 0 \\ \overline{\sigma_{11}} \\ \overline{\sigma_{12}} \\ \widetilde{u_1}\overline{\sigma_{11}} + \widetilde{u_2}\overline{\sigma_{12}} - \overline{q_1} \end{pmatrix}, \quad R_2 = \begin{pmatrix} 0 \\ \overline{\sigma_{12}} \\ \overline{\sigma_{22}} \\ \widetilde{u_1}\overline{\sigma_{12}} + \widetilde{u_2}\overline{\sigma_{22}} - \overline{q_2} \end{pmatrix}, \tag{5}$$

where $\overline{\sigma}$ represents the viscous and turbulent stress tensor (less the normal stress $\frac{2}{3}\overline{\rho}\widetilde{k}$) and $\overline{q}$ the heat flux vector given by:

$$\begin{cases} \overline{\sigma_{11}} = \left(\dfrac{1}{Re} + \mu_t\right)\left(2\dfrac{\partial \widetilde{u_1}}{\partial x_1} - \dfrac{2}{3}\left(\dfrac{\partial \widetilde{u_1}}{\partial x_1} + \dfrac{\partial \widetilde{u_2}}{\partial x_2}\right)\right), \\ \overline{\sigma_{22}} = \left(\dfrac{1}{Re} + \mu_t\right)\left(2\dfrac{\partial \widetilde{u_2}}{\partial x_2} - \dfrac{2}{3}\left(\dfrac{\partial \widetilde{u_1}}{\partial x_1} + \dfrac{\partial \widetilde{u_2}}{\partial x_2}\right)\right), \\ \overline{\sigma_{12}} = \left(\dfrac{1}{Re} + \mu_t\right)\left(\dfrac{\partial \widetilde{u_1}}{\partial x_2} + \dfrac{\partial \widetilde{u_2}}{\partial x_1}\right), \end{cases} \tag{6}$$

$$\begin{cases} \overline{q_1} = \left(\dfrac{\gamma}{RePr} + \dfrac{\gamma\mu_t}{Pr_t}\right)\dfrac{\partial \tilde{e}}{\partial x_1} + \dfrac{\mu_t}{\sigma_t}\dfrac{\partial \tilde{k}}{\partial x_1}, \\ \overline{q_2} = \left(\dfrac{\gamma}{RePr} + \dfrac{\gamma\mu_t}{Pr_t}\right)\dfrac{\partial \tilde{e}}{\partial x_2} + \dfrac{\mu_t}{\sigma_t}\dfrac{\partial \tilde{k}}{\partial x_2}. \end{cases} \tag{7}$$

The non-dimensional turbulent eddy viscosity is defined by:

$$\mu_t = C_\mu \frac{\overline{\rho}\widetilde{k}^2}{\widetilde{\varepsilon}}. \tag{8}$$

All the quantities have been non dimensionalized using a characteristic velocity scale U_0 and a characteristic length scale L. Re denotes the Reynolds number and Pr is the Prandtl number, which is equal to 0·72 for air. Pr_t is the turbulent Prandtl number, classically chosen as 0·9, γ is the ratio of specific heats (1·4 for air) and σ_k is a constant of the k-ε model (chosen as 1·0).

To use the Euler solver of Roe, a change of variable is introduced on the pressure and on the total energy to keep the hyperbolic part of the equations unchanged. The turbulent kinetic energy is added to the mean pressure term to define a new pressure p^* called effective pressure:

$$p^* = \overline{p} + \frac{2}{3}\overline{\rho}\widetilde{k} \tag{9}$$

and to the total energy, to define a new total energy E^*

$$E^* = \overline{E} + \left(-1 + \frac{2}{3(\gamma - 1)}\overline{\rho}\widetilde{k}\right). \tag{10}$$

2.2. *Equations for the turbulence scales*

To close the system of equations for the mean quantities (2), two additional transport equations may be solved for $\widetilde{k}$ and $\widetilde{\varepsilon}$. The modelled equations for $\widetilde{k}$ and $\widetilde{\varepsilon}$ can be written in conservative form as

$$\frac{\partial W'}{\partial t} + \operatorname{div}(F') = \operatorname{div}(R') + H', \tag{11}$$

where the vector variable W', the convective fluxes vector $F' = [F'_1, F'_2]$ and the diffusion fluxes vector $R' = [R'_1, R'_2]$ are given by:

$$W' = \begin{pmatrix} \bar{\rho}\tilde{k} \\ \bar{\rho}\tilde{\varepsilon} \end{pmatrix}, \quad F'_1 = \begin{pmatrix} \bar{\rho}\tilde{u}_1\tilde{k} \\ \bar{\rho}\tilde{u}_1\tilde{\varepsilon} \end{pmatrix}, \quad F'_2 = \begin{pmatrix} \bar{\rho}\tilde{u}_2\tilde{k} \\ \bar{\rho}\tilde{u}_2\tilde{\varepsilon} \end{pmatrix}, \tag{12}$$

$$R'_1 = \begin{pmatrix} \left(\frac{1}{Re} + \frac{\mu_t}{\sigma_t}\right)\frac{\partial \tilde{k}}{\partial x_1} \\ \left(\frac{1}{Re} + \frac{\mu_t}{\sigma_t}\right)\frac{\partial \tilde{\varepsilon}}{\partial x_1} \end{pmatrix}, \quad R'_2 = \begin{pmatrix} \left(\frac{1}{Re} + \frac{\mu_t}{\sigma_t}\right)\frac{\partial \tilde{k}}{\partial x_2} \\ \left(\frac{1}{Re} + \frac{\mu_t}{\sigma_t}\right)\frac{\partial \tilde{\varepsilon}}{\partial x_2} \end{pmatrix}. \tag{13}$$

The vector source term H' corresponds to a production and a dissipation term, given by

$$H' = \begin{pmatrix} \bar{\rho}P - \bar{\rho}\tilde{\varepsilon} \\ C_{\varepsilon_1}\bar{\rho}(\tilde{\varepsilon}/\tilde{k})P - C_{\varepsilon_2}\bar{\rho}(\tilde{\varepsilon}^2/\tilde{k}) \end{pmatrix}, \tag{14}$$

where P is the production of turbulent kinetic energy by the mean flow given by

$$P = -\frac{1}{\bar{\rho}}\left(\frac{2}{3}\bar{\rho}\tilde{k}\delta_{ij} - \mu_t\left(\frac{\partial \tilde{u}_i}{\partial x_j} + \frac{\partial \tilde{u}_j}{\partial x_i} - \frac{2}{3}\frac{\partial \tilde{u}_k}{\partial x_k}\delta_{ij}\right)\right)\frac{\partial \tilde{u}_i}{\partial x_j}. \tag{15}$$

The classical values of the constants are chosen:

$$C_\mu = 0{\cdot}09, \quad \sigma_k = 1{\cdot}0, \quad \sigma_\varepsilon = 1{\cdot}3, \quad C_{\varepsilon_1} = 1{\cdot}44, \quad C_{\varepsilon_2} = 1{\cdot}92.$$

The above models have been proposed initially for incompressible flows.[5] Some simulations have proved that the classical k-ε model doesn't predict important characteristics of compressible flows, such as the reduced growth rate of the mixing layer. For compressible flows, additional terms appear in the exact equations of $\tilde{k}$ and $\tilde{\varepsilon}$. Different modelings of those terms exist,[15,16] to take into account the effect of compression on the turbulence (as in a shock) and the effect of compressibility (as in a supersonic turbulent mixing layer). Some of these models have been tested,[17] and we have chosen the model of Coleman–Mansour,[16] which introduces an additional production term in the $\tilde{\varepsilon}$ equation in terms of the divergence of the mean flow (compression effect) and an additional compressible dissipation in the $\tilde{k}$ equation in terms of a turbulent compressible Mach number.

2.3. Wall functions

The derivation of the above turbulence transport equations is made under the hypothesis of high Reynolds number flows. Thus, in regions close to the wall, such as in the viscous sublayer where molecular effects are important, these equations are not valid and wall functions[6] are used to model this near wall region. The equations for the mean flow and the turbulence scales are solved up to a distance δ away from the wall. Near the wall, the flow is assumed to obey wall laws obtained from an integration of the boundary layer equations. By introducing the dimensionless wall distance y^+ and the friction velocity u_f:

$$u_f = \bar{\rho}u_f y/\mu. \tag{16}$$

The wall laws can be written as

$$\begin{cases} \dfrac{\tilde{u}.t}{u_f} = y^+ \text{ if } y^+ < 11{\cdot}6, \\ \dfrac{\tilde{u}.t}{u_f} = \dfrac{1}{K}\log(y^+) + C \text{ if } y^+ > 11{\cdot}6, \end{cases} \tag{17}$$

where $\tilde{u}.t$ is the tangential velocity. The constants of the logarithmic law are the Von Karman universal constants K and C respectively equal to 0·419 and 5·445. For the turbulent quantities, equilibrium between the production and the dissipation rate gives the proper boundary conditions:

$$\tilde{k} = \frac{u_f^2}{\sqrt{C_\mu}} \quad \tilde{\varepsilon} = \frac{u_f^3}{\delta K}. \tag{18}$$

Those laws have been established for incompressible flows but experiments with the compressible boundary layer[18] show that they remain valid in the absence of strong density variation.

3. NUMERICAL RESOLUTION

3.1. MUSCL method for the mean flow equations

The computational domain is divided into triangular elements to build a finite element mesh. Finite volume cells are constructed around each vertex by joining the inertial centers of the neighbouring triangles with the middles of the sides (Figure 1). The interpolation uses the classical P^1 basis functions N_i (piecewise linear on the finite element mesh) and the finite volume functions ϕ_j (the characteristic function of the cells C_i)

$$\phi_i(M) = 1, \quad M \in C_i, \quad \phi_i(M) = 0, \quad M \notin C_i. \tag{19}$$

The use of a flux splitting technique requires a finite volume discretization of the hyperbolic part of the equations (using a test function ϕ_i). The diffusive and the source terms are discretized using a Galerkin

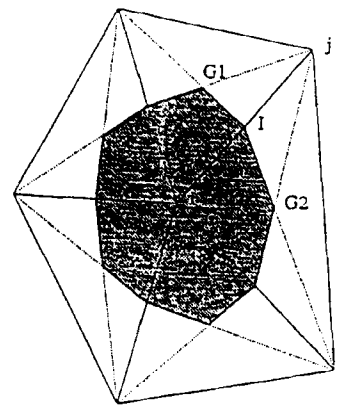

Figure 1. Barycentric cell around a vertex

method with a finite element interpolation (using a test function N_i). The discrete variational formulation of (2) is then written as

$$\int_\Omega \left(\frac{\partial W}{\partial t} + \mathrm{div}(F)\right)\phi_i \, \mathrm{d}s = \int_\Omega \mathrm{div}(R) N_i \, \mathrm{d}s, \tag{20}$$

which gives, after integration by parts,

$$\int_{C_i} \frac{\mathrm{d}W_i}{\mathrm{d}t} \, \mathrm{d}s + \int_{\partial C_i} F(W) \, \mathrm{d}l = -\int_\Omega R.\mathrm{grad}(N_i) \, \mathrm{d}s + \int_\Gamma R.n \, N_i \, \mathrm{d}l. \tag{21}$$

With a centred discretization for the convective terms, this formulation is equivalent to a full Galerkin finite element formulation[14] with a mass lumping technique for the time derivative term. The upwinding discretization is obtained by using a Roe's flux splitting[9] technique, which is an upwind scheme along the characteristic lines. This solver is one of the simplest and more accurate scheme for supersonic flows up to a Mach number of 3. Its spatial precision is only first order accurate which entails a great numerical diffusivity. A second order scheme is obtained with a MUSCL method introduced by Van Leer[19,20] using an approximate gradient of W at each vertex, derived from the Galerkin linear interpolation of W over all the neighbouring triangles. To preserve the TVD property of this scheme, a Van Albada–Van Leer limiter is used.[20] Turbulence equations are similarly discretized using a mixed finite volume/finite element method

$$\int_{C_i} \frac{\mathrm{d}W_i'}{\mathrm{d}t} \mathrm{d}s + \int_{\partial C_i} F'(W') \, \mathrm{d}l = -\int_\Omega R'.\mathrm{grad}(N_i) \, \mathrm{d}s + \int_\Gamma R'.n \, N_i \, \mathrm{d}l. \tag{22}$$

The flux over the boundary ∂C_i of the cell i is the sum of the fluxes over the intersection ∂C_{ij} of the cell i and each of its neighbouring cell j:

$$\int_{\partial C_i} F'(W').n \, \mathrm{d}l = \sum_{j \text{ neighbours of } i} \int_{\partial C_{ij}} F'(W').n \, \mathrm{d}l. \tag{23}$$

The convective fluxes between two neighbour cells C_i and C_j (Figure 2) are calculated using the mass flux

$$\int_{\partial C_{ij}} \widetilde{\rho u}.nW' \, \mathrm{d}s = W_i' \int_{\partial C_{ij}} \widetilde{\rho u}.n \, \mathrm{d}s \quad \text{if} \quad \int_{\partial C_{ij}} \widetilde{\rho u}.n \, \mathrm{d}s > 0, \tag{24}$$

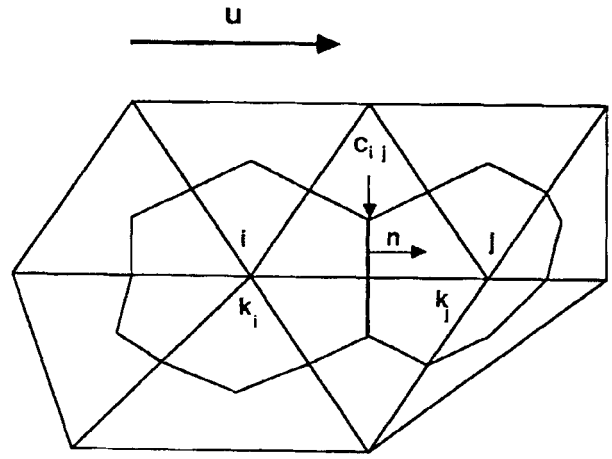

Figure 2. Intersection between two neighbour cells C_i and C_j

$$\int_{\partial C_{ij}} \overline{\rho}\widetilde{u}.nW' \, ds = W'_j \int_{\partial C_{ij}} \overline{\rho}\widetilde{u}.n \, ds \quad \text{if} \quad \int_{\partial C_{ij}} \overline{\rho}\widetilde{u}.n \, ds < 0. \tag{25}$$

The viscous terms and the source terms are discretized using the finite element formulation.

3.2. *Time stepping*

Steady solutions of the system (2), (11) are sought by an unsteady process. The time integration uses an explicit four-steps Runge–Kutta method and a local time step given by a local Courant condition. At each time step, the mean flow equations are first solved and then the turbulence scales equations. The computations are performed on an Alliant 2800 using a single processor. With the explicit scheme, it takes several hours of cpu time to converge starting from constant initial fields for a mesh with 4000 nodes (compression ramp). An implicit scheme is under development to reduce that computational time.

3.3. *Boundary conditions*

The computational domain is bounded by an inflow boundary, an outflow boundary, a free boundary and a wall boundary. The boundary conditions are not imposed as Dirichlet conditions but are used to compute the fluxes and the stresses on the boundaries.

(i) On the free boundaries, a zero flux condition is applied for the velocity.

(ii) To calculate the inflow fluxes, farfield values deduced from the experiments are introduced. The convective fluxes are calculated from the farfield values and from the inner values using a Steger–Warming splitting. The viscous fluxes are assumed to be negligible. Outflow fluxes are similarly computed but in the farfield, all the values except the pressure are set equal to the inner values.

(iii) On the wall, boundary conditions for the velocity are imposed through the variational formulation. A first estimation of the skin velocity u_f is computed from the tangential velocity using the linear law.

$$u_f = \sqrt{\frac{\mu \widetilde{u}.t}{\overline{\rho}\delta}} \tag{26}$$

If $y^+ > 11{\cdot}6$ a new evaluation of u_f is computed from the logarithmic law (17) using a Newton method. Knowing the skin velocity, the viscous stress $\tau_p = \overline{\rho}u_f^2$, which appears in the variational formulation of the equations (21) (term $R.n$), is imposed on each cell boundary Γ_i.

$$\int_{\Gamma_i} \tau_p.tN_i \, dl = \int_{\Gamma_i} \overline{\rho}u_f^2.tN_i \, dl \tag{27}$$

For $\widetilde{k}$ and $\widetilde{\varepsilon}$, the relations (18) are used as Dirichlet boundary conditions.

4. NUMERICAL RESULTS

4.1. *Turbulent flow over a backward facing step*

The first validation test case is the classical flow over a backward facing step. Experimental data from Kim *et al.*[21] are also available. Comparisons have been done with numerical data obtained on the same mesh using an incompressible finite element method.[22] The computational domain and the finite

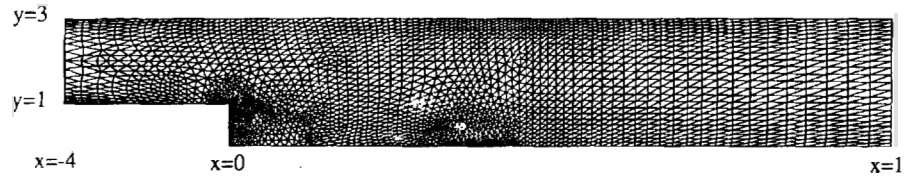

Figure 3. Geometry of the backward facing step and finite element mesh (2101 nodes)

element mesh are drawn in Figure 3. The velocity U_o at the entrance of the pipe is equal to 18 m/s and the Reynolds number is equal to 44580. To simulate an incompressible flow, the computation is done with a small Mach number of 0·1. The results are non dimensionalized by the velocity at the entrance U_o and by the height of the step h. As the flow is incompressible, the classical k-ε model is used in the calculation.

The flow presents a recirculation bubble behind the step. Streamlines in the recirculation bubble are shown in Figure 4. The two calculations predict the same recirculation length with a lower velocity in the bubble in our results. This length ($L \approx 5h$) is underpredicted with regard to the experimental length ($L \approx 7h$). Numerous numerical simulations have already shown that the classical k-ε model with wall functions underpredicts the length of the recirculation. On the one part, the Boussinesq hypothesis is no more valid when the streamlines are too curved and on the other part, the wall laws don't take into account the pressure gradient which is important in the reattachment region. The transversal velocity and kinetic energy profiles are plotted in two sections: ($x = 5{\cdot}3h$, $x = 10{\cdot}7h$) for the velocity and $x = 7{\cdot}7h$, $x = 10{\cdot}3$) for the kinetic energy (Figures 5–8). The two numerical results are in reasonable agreement. The under prediction of the recirculation bubble produces a gap between the experimental and the numerical results in the downstream profiles.

4.2. Compression ramp

The compression ramp is a complex test case which embodies all the difficulties of turbulence with a shock/boundary layer interaction and compressibility effects. This problem has practical applications in aerothermodynamic and in turbomachinery. This test case has been chosen to test the capacity of the method to predict the correct shock and the recirculation bubble induced by the shock/boundary layer interaction. Experiments have been done by Settles[23] for the two dimensional interaction generated by compression ramps with different angles. In this article, two angles are considered: 8° and 24°. The uniform freestream conditions correspond to a Mach number equal to 2·85 and a Reynolds number equal to $1{\cdot}7 \times 10^6$. The incoming turbulent boundary layer thickness δ_0 is nearly equal to 2·3 cm and the skin friction coefficient to 10^{-3}. In the case of the 8° ramp, there is a shock wave with no discernible flow separation. In the case of the 24° ramp, there is a separated region and a detached shock wave in the front of the ramp. The extend of the recirculation zone as measured along the model surface is slightly more than twice the incoming boundary layer thickness.

The shape of the computational domain is shown on Figure 9. The inflow boundary is located ahead of the corner in a region of no upstream influence ($10\delta_0$) and the outflow boundary is chosen

Figure 4. Streamlines in the recirculation bubble

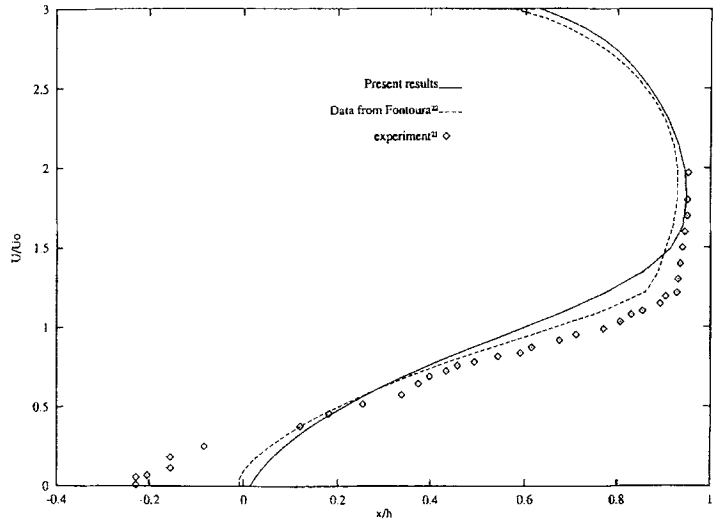

Figure 5. Mean axial velocity profiles at $x = 5{\cdot}3h$

sufficiently far from the corner ($7\delta_0$). The height of the computional domain ($12\delta_0$) is chosen so that freestream conditions apply along the upper boundary. The upstream boundary conditions are obtained from a calculation of the development of a flat plate turbulent boundary layer with a skin friction coefficient of 10^{-3}. A mesh with 2400 nodes is used in the 8° case and a mesh, refined in the boundary layer (Figure 10), is used in the 24° case. In the 24° case, to improve the results, computations have also been done with the Coleman–Mansour[15] k-ε model.

For the 8° case, comparisons with the experimental wall pressure are shown in Figure 11 and the computed and experimental skin frictions distribution in Figure 13. For the pressure, the agreement with experimental data is good. The angle of the shock (26°) is in good agreement with the theoretical angle given by the Euler theory, indicating that the Roe solver calculates the shock precisely. The

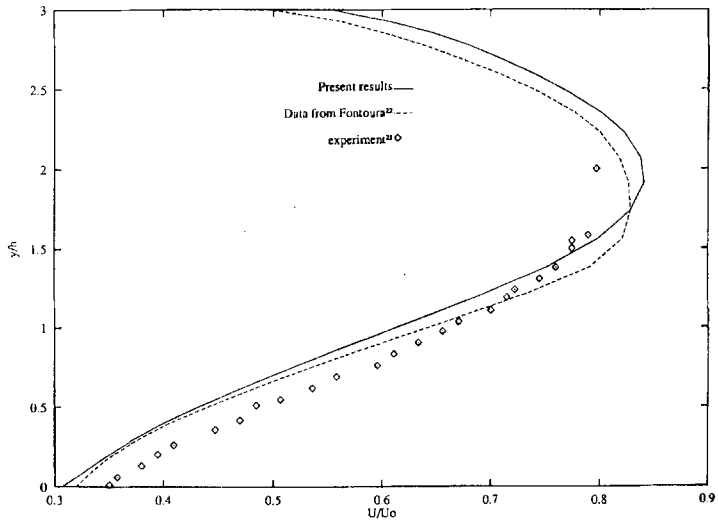

Figure 6. Mean axial velocity profiles at $x = 10{\cdot}7h$

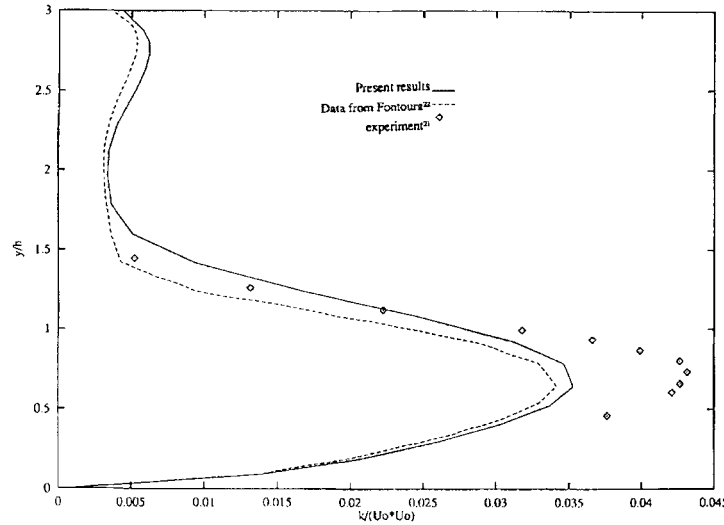

Figure 7. Turbulent kinetic energy profiles at $x = 7{\cdot}7h$

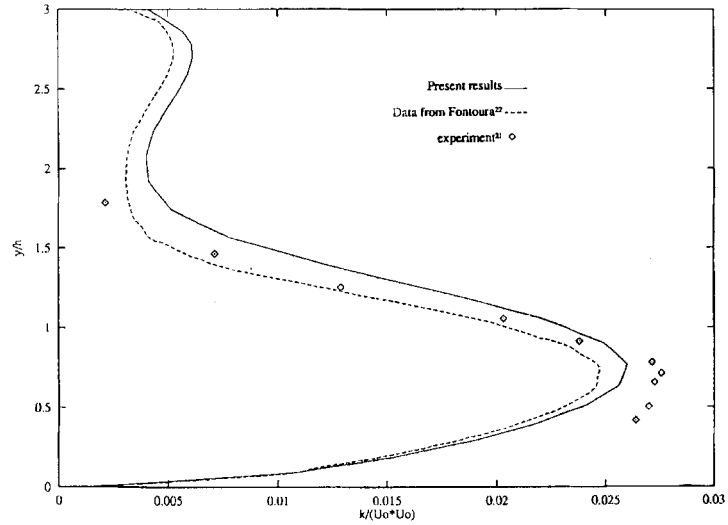

Figure 8. Turbulent kinetic energy profiles at $x = 10{\cdot}3h$

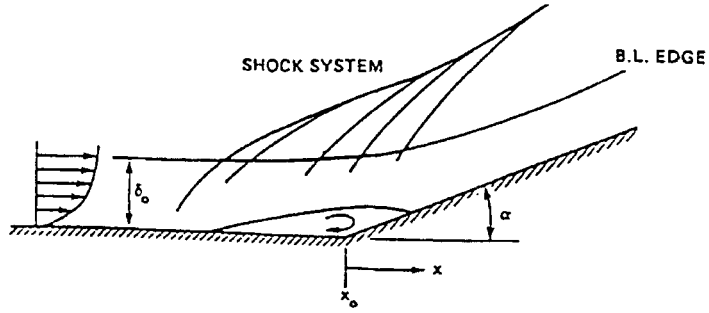

Figure 9. Sketch of supersonic compression corner shock-wave boundary layer-interaction experiment

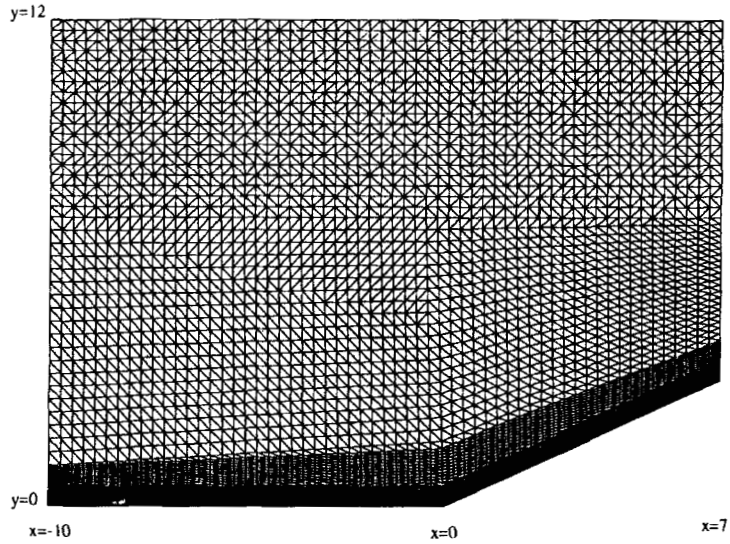

Figure 10. The finite element mesh for the 24° compression ramp (5886 nodes)

computed outgoing skin friction coefficient C_f values are higher than the experimental values. For the 24° case, the wall pressure and the skin friction distributions are respectively presented in Figures 12 and 14. The numerical values of Viergas *et al.*[4] have also been plotted. The pressure plateau due to the separated region is underpredicted by the k-ε model. The Coleman–Mansour model gives a better prediction for the location of the separation. The angle of the shock is also in good agreement with the Euler theory. Measured and computed velocity in three different sections are shown on the Figures 15, 16, 17. The numerical profiles are retarded in comparison with the experimental profiles, although the results are slightly better with the Coleman–Mansour model. This comportment has been already noticed by Viergas *et al.*[4] for the two equations models. It is an indication that the k-ε model with wall functions does not predict well the recovery region.

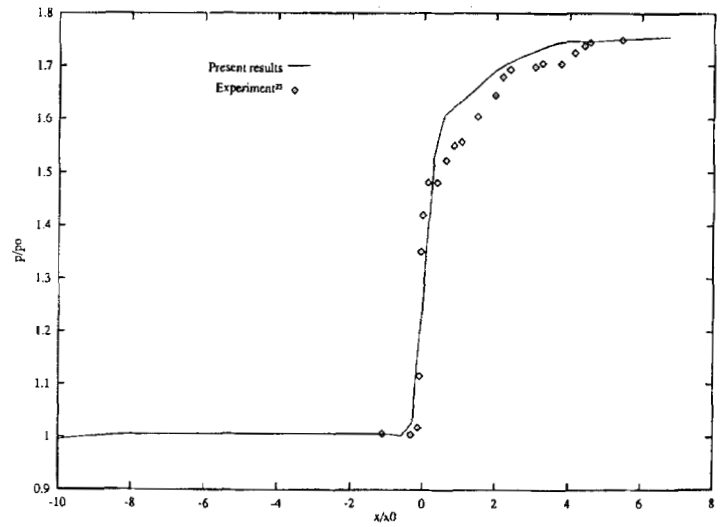

Figure 11. Comparison of experimental surface static pressure with computations for the 8° compression ramp

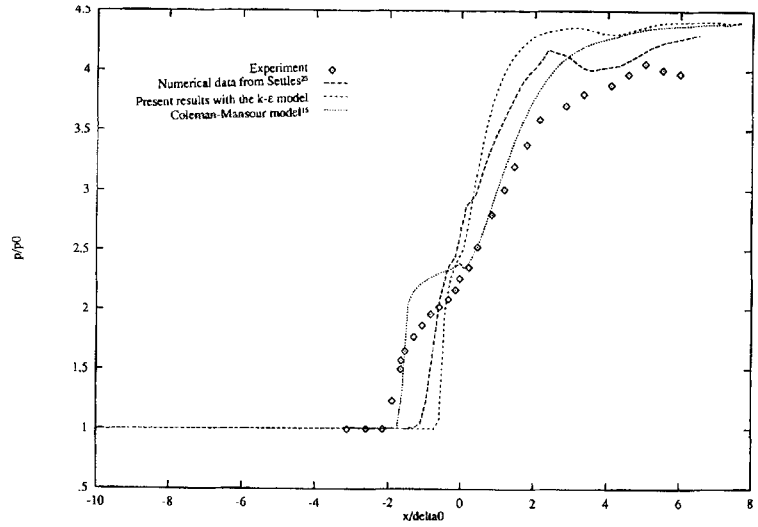

Figure 12. Comparison of experimental surface static pressure with computations for the 24° compression ramp

Those results prove the capacity of the numerical method to predict compressible turbulent flows with shocks. To improve the prediction in the 24° case new models must be tested (low Reynolds models and new compressible terms).

5. CONCLUSION

A numerical method to solve turbulent compressible flows has been described. The turbulence is modeled by a k-ε model with wall functions. The numerical method is an extension of a finite volume/finite element method developed to solve the Euler equations. A special treatment of the boundary conditions at the solid walls is introduced in the variational formulation. Then, two validation turbulent test cases are presented: an incompressible flow over a backward facing step to validate the classical k-ε

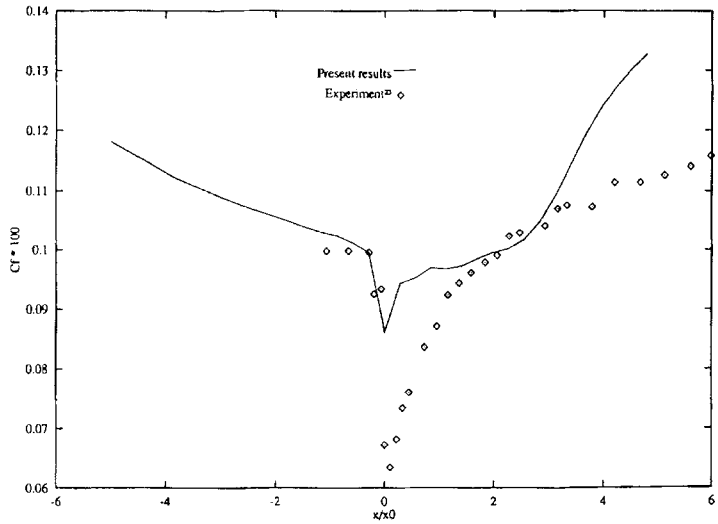

Figure 13. Comparison of experimental skin friction distributions with computations for the 8° compression ramp

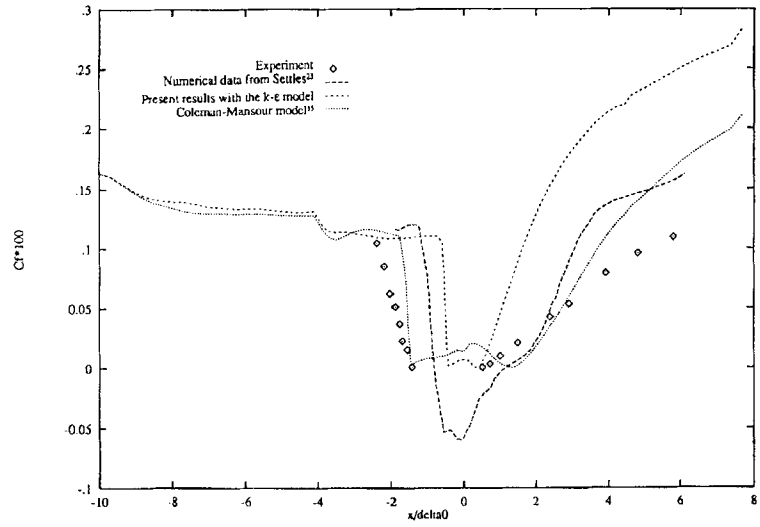

Figure 14. Comparison of experimental skin friction distributions with computations for the 24° compression ramp

model and a supersonic flow over a compression ramp to validate an extension of the k-ε model for compressible flows. Comparisons have been performed with experimental and numerical data. The principal characteristics of the flow are well predicted (the shock waves and the separated regions) and our results are in reasonable agreement with the other numerical results. But failure of the classical k-ε models to predict recovery regions indicates that the turbulent model need to be improved in those regions. The extension of the k-ε model for compressible flows is very promising and allow this numerical technique to be used to predict complex compressible flows as in the combustion chamber of gas turbine engines. However, to improve the numerical efficiency of the method, an implicit scheme is under development. To improve the prediction, new turbulent models are also tested, especially for the near wall region (low Reynolds k-ε models).

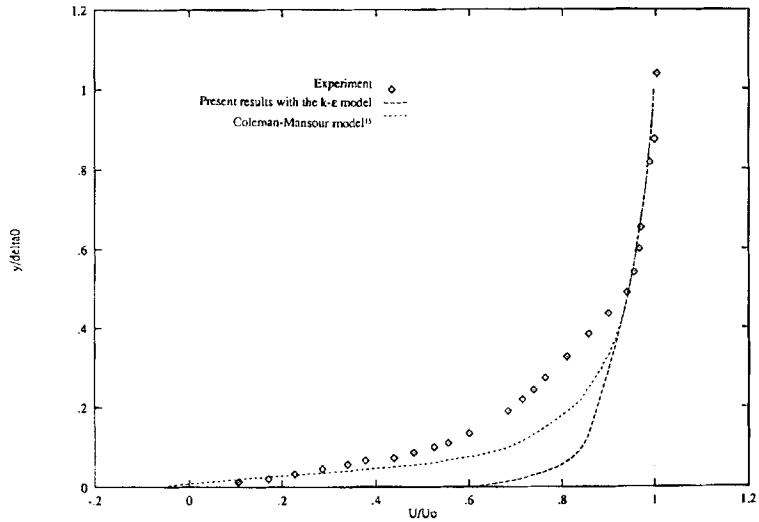

Figure 15. Comparison of computations and velocity profiles measurements for the 24° compression ramp at the section $x = -1{\cdot}45$

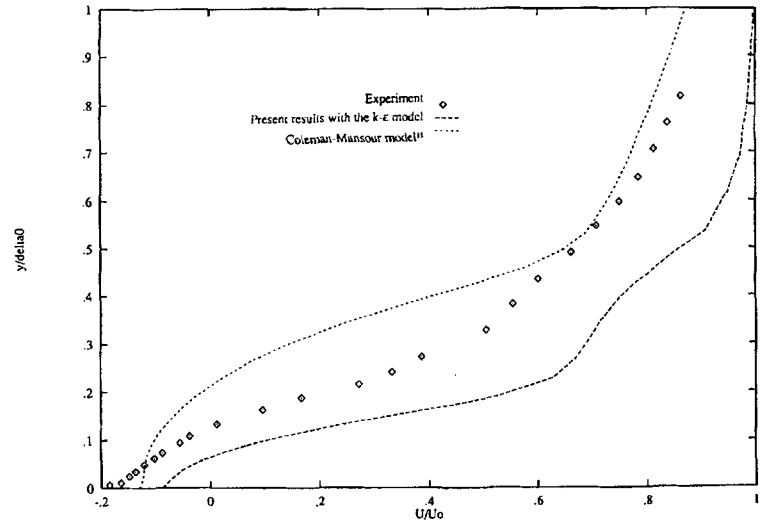

Figure 16. Comparison of computations and velocity profiles measurements for the 24° compression ramp at the section $x = 0$

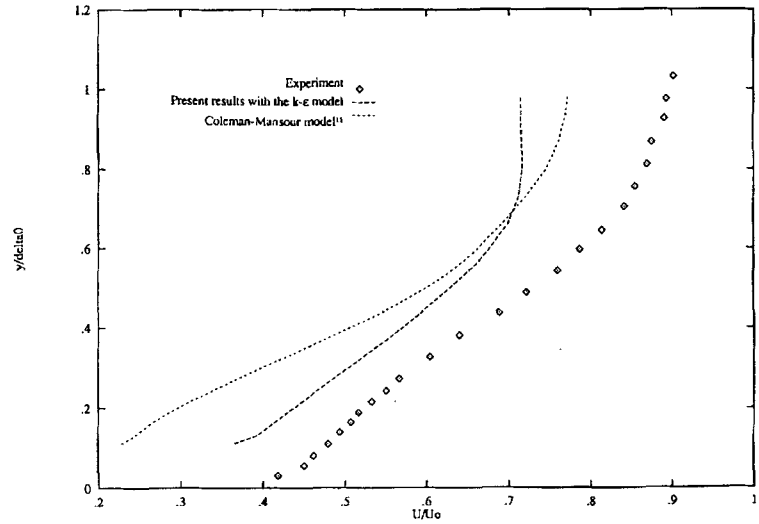

Figure 17. Comparison of computations and velocity profiles measurements for the 24° compression ramp at the section $x = 2{\cdot}89$

REFERENCES

1. G. Brun, M. Buffat, S. Aubert and J. L. Schultz, 'Numerical simulation of the 3D turbulent flow around the combustor dome of an aircraft engine', in *Proc. First European computational fluid dynamics conf.*, Brussels, 7–11 September, 1992.
2. M. Visbal and D. Knight, 'The Baldwin–Lomax turbulence model for two-dimensional shock-wave/boundary-layer interactions', *AIAA J.*, **22** (1984).
3. B. Escande and L. Cambier, 'Validation du code CANARI par le calcul de l'écoulement tridimensionnel turbulent dans un distributeur de turbine', *10e Congrès Français de Méecanique*, Paris, 2–6 Septembre, 1991.
4. J. R. Viegas and C. C. Horstmann, 'Comparison of multiequation turbulence models for several shock boundary-layer interaction flows', *AIAA J.*, **17** (1979).
5. B. E. Launder and D. B. Spalding, '*Mathematical models of turbulence*', Academic Press, London, 1972.
6. T. Cebeci and A. M. O. Smith, '*Analysis of turbulent boundary layer*', Academic Press, 1974.

7. J. Steger and R. F. Warming, 'Flux vector splitting for the inviscid gas dynamic with applications to finite difference methods', *J. Comp. Phys.*, **40**, 263–293 (1981).
8. R. M. Mc Cormak, 'A numerical method for solving the equations of compressible viscous flows', *AIAA J.*, **20**, 1275–1281 (1982).
9. P. L. Roe, 'Approximate Riemann solvers, parameters vectors and difference schemes', *J. Comp. Phys.*, **43**, 357–371 (1981).
10. D. J. Mavriplis and L. Martinelli, 'Multigrid solution of compressible turbulent flow on unstructured meshes using a two equations model', *29th Aerospace Sciences Meeting*, Rena, Nevada, January 7–10, 1991.
11. F. Chalot, Z. Johan, M. Mallet, M. Ravachol and G. Rog, 'Development of a finite element Navier–Stokes solver with applications to turbulent and hypersonic flows', *30th Aerospace Science Meeting and Exhibit*, Reno, January 6–9, 1992.
12. A. Dervieux, 'Steady Euler simulations using unstructured meshes', *VKI*, Lectures series 1884-04, 1985.
13. D. Jeandel, M. Buffat, G. Brun, C. Le Ribault, Y. Mao, A. Dervieux, L. Fezoui, S. Lanteri, B. Larrouturou and C. Olivier, 'Finite element method and turbulence modeling for internal flows', *GAMNI-SMAI-IMA Conference on Computational aeronautical dynamics*, Antibes, May 17–19, 1989.
14. H. Steve, 'Schémas implicites linéaires décentrés pour la résolution des equations d'Euler en plusieurs dimensions', Thèse Université de Provence Aix-Marseille, 1988.
15. G. N. Coleman and N. N. Mansour, 'Simulation and modeling of homogeneous compressible turbulence under isotropic mean compression', *Eight Symposium on turbulent shear flows*, Université Technique de Munich, 1991.
16. S. Sarkar and B. Lakshmanan, 'Application of a Reynolds stress turbulence model to the compressible shear layer', *AIAA J.*, **29**, 743–749 (1991).
17. C. Le Ribault, M. Buffat and D. Jeandel, 'Numerical investigation of supersonic turbulent flows by a mixed finite volume/ finite element method', in *Proc. First European computational fluid dynamics conf.*, Brussels, 7–11 September, 1992.
18. M. Elena and J. P. Lacharine, 'Experimental study of a supersonic turbulent boundary layer using a laser Doppler anemometer', *Jour. Mec. Th. Appl.*, **7**, 175–190 (1988).
19. B. Van Leer, 'Computational methods for ideal compressible flows', *Cours Von Karman Institute, Lectures Series*1983–1984 *computational fluid dynamic*, 1983.
20. L. Fezoui, 'Résolution des équations d'Euler par un schéma de Van Leer en éléments finis', *Rapport de Recherche INRIA*, n358, 1985.
21. J. Kim, S. J. Kline and J. P. Johnson, 'Investigation of a reattaching turbulent shear layer: flow over a backward-facing step', *Trans. ASME, J. Fluid Engineering*, **102** (1980).
22. J. Fontoura, 'Méthode de minimisation adaptée à la technique des éléments finis pour la simulation des écoulements turbulents avec conditions aux limites non linéaires de proche paroi', *Thèse Ecole Centrale de Lyon*, 1990.
23. G. S. Settles, T. J. Fizpatrick and S. M. Bogdonoff, 'Detailed study of attached and separated compression corner flowfields in high Reynolds number supersonic flow', *AIAA J.* **17** (1979).
24. C. Olivier, 'Simulation numérique d'écoulements visqueux compressibles laminaires et turbulents', *Thèse Université de Nice*, 1990.